Generation of isolated attosecond electron sheet via relativistic spatiotemporal optical manipulation

Fengyu Sun,[1,2,3] Wenpeng Wang [1,*] Hao Dong,[1,3] Jianzhi He,[1,2,3] Zhiyong Shi,[1] Zhengxing Lv,[1,3] Qiwen Zhan [4]
Yuxin Leng,[1,2] Songlin Zhuang,[4] and Ruxin Li[1,2,†]

[1]*State Key Laboratory of High Field Laser Physics and CAS Center for Excellence in Ultra-intense Laser Science,*
Shanghai Institute of Optics and Fine Mechanics (SIOM), Chinese Academy of Sciences (CAS), Shanghai 201800, China
[2]*School of Physical Science and Technology, ShanghaiTech University, Shanghai 201210, China*
[3]*University of Chinese Academy of Sciences, Beijing 100049, China*
[4]*School of Optical-Electrical and Computer Engineering,*
University of Shanghai for Science and Technology, Shanghai 200093, China

Novel phase-locked acceleration of a relativistic isolated attosecond electron sheet was realized using a relativistic reflected spatiotemporal optical vortex (STOV) pulse in three-dimensional particle-in-cell simulations. Electrons can be trapped in a spatiotemporal phase singularity within the STOV pulse center, modulated into an approximately 600-attosecond duration sheet. Furthermore, electrons can be phase-locked accelerated to the order of GeV in the longitudinal direction. Such an isolated attosecond electron sheet driven by the intense STOV pulse can be used in isolated attosecond pulse generation, ultrashort x/γ-ray radiation, and attosecond electron diffraction.

I. INTRODUCTION

Optical vortices are fundamental optics phenomena that refer to localized regions where the energy flow of an electromagnetic field circulates around an axis. They are characterized by the expression $\exp(-il\varphi)$ in mathematics, which endows light fields with optical orbital angular momentum (OAM), $l\hbar$ [1]. Here, l is an integer that is known as the topological charge, $\hbar$ is the Dirac constant, and φ is the azimuthal angle, which determines a phase singularity and the zero-intensity amplitude distribution in the beam center. At present, optical vortices are primarily divided into spatial vortices and spatiotemporal vortices (STOVs), depending on the space and time variables of φ. Spatial optical vortices carry the longitudinal (space-varying) OAM with the expression $\exp[-il\varphi(x, y)]$, parallel to the laser propagating direction (z axis) of the beam [1], which can be realized by using transmitted phase plates. STOVs carry the transverse (time-varying) OAM with the expression $\exp[-il\varphi(x, y, z, t)]$, perpendicular to the laser propagating direction [2]. They can be realized by using an additional transmission grating and a cylindrical lens to add the spiral phase in the spectral domain [3–6]. Based on the special OAM and intensity singularity charac-

teristics of optical vortices, they have been widely applied in optical manipulations [7,8], optical communications [9,10], microscopy and imaging [11,12], astrophysics [13], and time-varying OAM generation [14–16]. However, these optical vortices were mostly limited to weak laser fields because their transmission optical components have a low damage threshold that could be destroyed when high-power lasers pass through them.

With the rapid development of superintense ultrafast laser technology, laser intensities have exceeded 10^{22} W/cm^2 [17,18], allowing the matter interaction to go into the laser-driven plasma interaction region. Here, fundamental particles such as electrons, ions, and photons are tuned for various applications, including particle acceleration [19–22], x-ray and γ-ray generation [23,24], and radiation generation [25,26]. It is believed that novel multidimensional manipulations may go into relativistic particle interactions when the vortex lights are extended from the previous nonrelativistic region to the new relativistic region (laser intensity usually $>10^{18}$ W/cm^2). For example, a large reflective phase plate was developed to generate an intense Laguerre-Gaussian pulse (spatial optical vortex) [19] for applications including collimated electron beam generation [22], proton acceleration [20,21], vortex harmonics generation [27–29], and x/γ-ray beam generation [23,24] in theories and simulations. However, to date, the intense STOV pulse has seldom been realized in the relativistic intensity region ($>10^{18}$ W/cm^2) because its high-intensity and high-flux light may destroy the transmission grating and cylindrical lens in the experimental optical path [3–5]. The realization of an intense STOV pulse using a reflection method similar to previous research [19] may bring another degree of spatiotemporal freedom to relativistic laser-driven plasma interactions.

*wangwenpeng@siom.ac.cn
†ruxinli@mail.siom.ac.cn

For example, the electron beam could be spatiotemporally modulated in the direct laser acceleration (DLA) regime [30–34] to improve its beam divergence and energy spectrum properties, bringing new insights into potential applications.

In this paper, we propose a relativistic STOV pulse using reflecting optical elements, such as diffraction gratings, cylindrical mirrors, and phase plates in a light path, to realize the modulation and acceleration of an isolated attosecond electron sheet in three-dimensional (3D) particle-in-cell (PIC) simulations. The spatiotemporal phase singularity of the STOV pulse is found to be crucial for concentrating electrons in temporal-spatial dimensions. In addition, the phase velocity in the longitudinal field of the STOV is close to the speed of light, thus aiding in the realization of phase-locked electron acceleration. Finally, for a 6.8 PW STOV laser, an isolated attosecond electron sheet with a duration of 670 attoseconds (as) and a charge of 65 pC is accelerated to the GeV order. Such a relativistic STOV pulse provides a new convenient method for accelerating a single attosecond electron sheet with broad applications in attosecond electron diffraction and microscopy [35–37], isolated attosecond pulse generation [38,39], ultrashort isolated x/γ-ray radiation [30,40–44], relativistic isolated electron mirrors [30,31,45], and other fields [32].

II. GENERATION OF RELATIVISTIC STOV PULSE

The concept of the reflected optical elements is used principally to generate the relativistic STOV pulse to circumvent the optical modulator damage limit of current relativistic laser-driven experiments. First, a 40-fs circularly polarized (CP) Gaussian pulse is incident onto a blazed grating with the electric field expression $E_1(x_1, y_1, \omega) = E_0 \exp[-(x_1^2 + y_1^2)/a^2 - (\omega - \omega_c)^2/b^2]$. Here, E_0 is the amplitude of the electric field, ω is the laser frequency, $\omega_c = 2\pi c/\lambda$ is the carrier frequency, c is the light velocity in vacuum, $\lambda = 1\,\mu m$ is the laser central wavelength, $a = 250\,mm$ is the radius of the laser spot, and $b = 40\,nm$ is the full width at half maximum of the spectral bandwidth. The blazed grating (1480 lines/mm, blaze wavelength 1 μm) [3,46] reflects and diffracts the Gaussian pulse in the spectrum to the first-order field with the expression $E_2(x_2, y_2, \omega) = E_1(\beta x_1, y_1, \omega) \exp[i\eta(\omega - \omega_c)x_2]$ [3,46]. Here, $\beta = \cos(\theta_i)/\cos(\theta_d)$, $\eta = 2\pi/\omega_c d\cos(\theta_d)$, and θ_i and θ_d are the incident and diffracted angles (for the central wavelength light) with respect to the grating normal, respectively. d is the periodicity of the grating. A cylindrical mirror (focal distance $f_c = 4\,m$) [3] is then used to focus the laser in the x dimension, which is expressed as $E_3(x_3, y_3, \omega) = \mathrm{IFT}\{\mathrm{FT}\exp[E_2(x_2, y_1, \omega)]\exp[2iz\pi c/\lambda - i\pi\lambda z(f_x^2 + f_y^2)]\}\exp(-ikx_3^2/2f_c)$. Here, FT and IFT denote the spatial Fourier transform and inverse Fourier transform, respectively, where f_x and f_y are spatial frequencies. Finally, a reflected phase plate adds the vortex $\exp[-il\tan^{-1}(y/x)]$ to the light in the frequency domain (k_x-ω plane) and reflects the light back to the previous cylindrical mirror and diffraction grating. In the reflection process, the vortex phase is inversely Fourier transformed to the spatial-temporal domain (t-x plane). Notably, the chirp is not an important parameter for the STOV pulse generation in our case, because the blazed gratings,
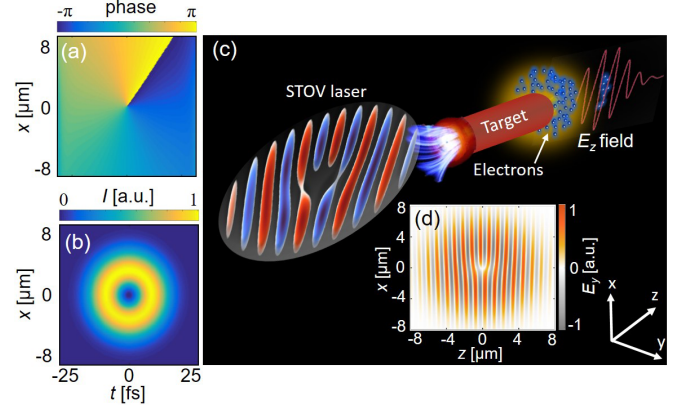

FIG. 1. (a) Phase and (b) intensity of the focal STOV pulse in the t-x plane. (c) Schematic diagram of the accelerating scheme. The STOV pulse is incident from the left and radiates onto the nanowire target. The electrons can be initially dragged out from the target and further phase locked and accelerated by the longitudinal electric field (E_z) inside the STOV laser. (d) E_y electric field of the STOV pulse in PIC simulations.

transversal mirrors, and phase plates do not bring chirp to the laser.

The STOV pulse can be further focused by an off-axis parabola ($f = 1\,m$) to form an intense STOV pulse with a spiral phase [see Fig. 1(a)] and a hollow intensity distribution [see Fig. 1(b)].

III. SIMULATION RESULTS

In 3D PIC simulations (EPOCH) [47], the relativistic STOV pulses are coupled to drive the nanowire target and generate a relativistic isolated attosecond electron sheet (RIAES). The STOV pulse can be expressed as

$$\boldsymbol{E}_x = E_0 \frac{w_0}{w}[(\xi/w)^2 + (x/w)^2]^{|l|/2}$$
$$\times \exp[-(\xi/w)^2 - (x/w)^2 - (y/w)^2]$$
$$\times \exp[i(-l\phi_{st} + kz - \omega t + \phi_0)]\exp(\boldsymbol{e}_x), \quad (1)$$

$$\boldsymbol{E}_y = E_0 \frac{w_0}{w}[(\xi/w)^2 + (x/w)^2]^{|l|/2}$$
$$\times \exp[-(\xi/w)^2 - (x/w)^2 - (y/w)^2]$$
$$\times \exp[i(-l\phi_{st} + kz - \omega t + \phi_0)]\exp\left(i\frac{\pi\sigma_z}{2}\boldsymbol{e}_y\right), \quad (2)$$

where $E_0 = a_0 m_e \omega c/e$, m_e is the electron mass, e is the electron charge, $a_0 = 70$ is the normalization amplitude of the laser pulse (corresponding to the laser intensity $I_0 = 2 \times 1.38 \times 10^{18} a_0^2 = 1.35 \times 10^{22}\,\mathrm{W/cm^2}$). Here, $\phi_{st} = \tan^{-1}(x/\xi)$ is the spatiotemporal plane azimuthal angle, $\xi = ct - z$ is a longitudinal coordinate local to the pulse, $w = w_0\sqrt{1 + (\frac{z}{z_R})^2}$ is the beam waist, $w_0 = 4\,\mu m$ is the full width at
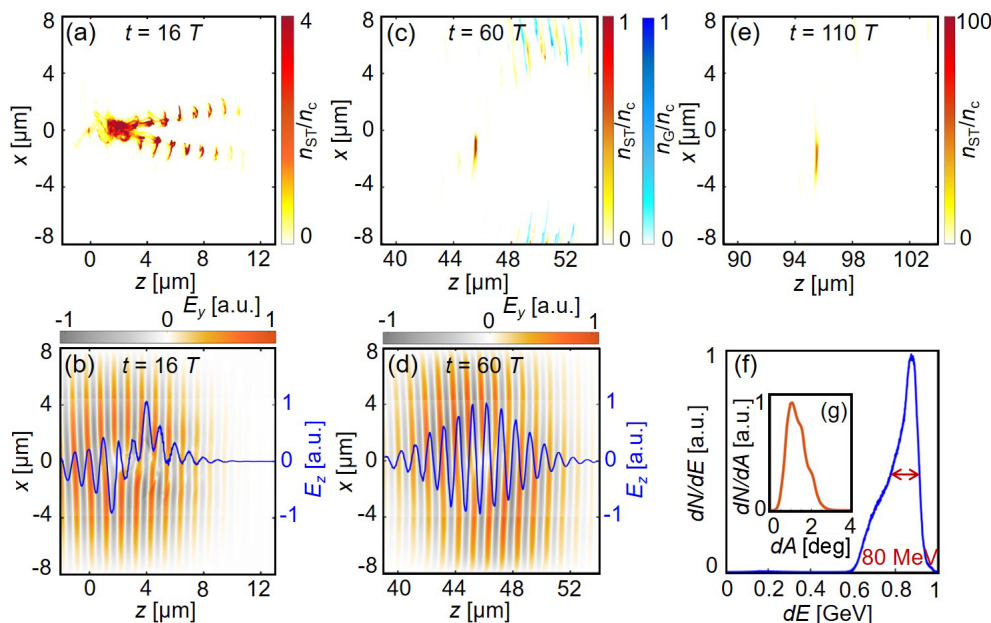
FIG. 2. Electron density n_{ST} driven by an STOV pulse at $t =$ (a) $16T$, (c) $60T$, and (e) $110T$. The electron density n_G driven by Gaussian pulse is compared in (c). The amplitude of the Gaussian pulse and the STOV pulse remain the same in (c). Electric field $\boldsymbol{E}_y$ and longitudinal electric field $\boldsymbol{E}_z$ (blue line) at (b) $t = 16T$ and (d) $t = 60T$ are plotted. The electron density is integrated from $-3\,\mu m < y < 3\,\mu m$ into the $x-z$ plane in (e) at $t = 110T$. (f) Energy spectra and (g) divergence of the electrons are calculated in the region $-3\,\mu m < x < 3\,\mu m$, $-3\,\mu m < y < 3\,\mu m$, and $95.5\,\mu m < z < 95.7\,\mu m$.

half maximum of the diameter of the focus spot, $z_R = \pi w_0^2/\lambda$ is the laser Rayleigh length, and $l = 1$ is the topological charge number, $\sigma_z = -1$ is the spin angular momentum, k is the wave number, and $\phi_0 = 0.1\pi$ is the initial phase. It should be noted that the STOV in our case is not tight focusing,

because the numerical aperture value $NA = n\sin(a/f) \sim 0.2$ is smaller than 0.7, where $n = 1$ is the refractive index [48]. The longitudinal electric field (E_z) offers an accelerating configuration near the z axis, which can be calculated from the Poisson equation $\boldsymbol{E}_z = -(i/k)(\partial\boldsymbol{E}_y/\partial y + \partial\boldsymbol{E}_x/\partial x)$,

$$\boldsymbol{E}_z = E_0 \frac{i}{k} \frac{w_0}{w} \exp\left[-\left(\frac{\xi}{w}\right)^2 - \left(\frac{x}{w}\right)^2 - \left(\frac{y}{w}\right)^2 + [i(-l\phi_{st} + kz - \omega t + \phi_0)]\right] \exp(\boldsymbol{e}_z)$$

$$\times \left[\left[\left(\frac{\xi}{w}\right)^2 + \left(\frac{x}{w}\right)^2\right]^{l/2} \left(\frac{2y}{w^2} + \frac{2x}{w^2} + \frac{iz}{z^2 + x^2}\right) - \frac{1}{2}\left[\left(\frac{\xi}{w}\right)^2 + \left(\frac{x}{w}\right)^2\right]^{-l/2} \frac{2x}{w^2}\right]. \quad (3)$$

The simulation box size is 15 μm (z)×16 μm (x)× 16 μm (y). There are $600 \times 640 \times 640$ cells, and the wire target is filled with 7.4×10^8 electrons and 7.4×10^8 protons. The intense STOV pulse propagates along the $+z$ axis from the left side of the simulation box, which is initialized by the boundary conditions at the box boundaries. The nanowire target with a diameter of 400 nm is initially located in the region of $0\,\mu m < z < 4\,\mu m$. The target density is $n_e = 100n_c$, where the classical critical density $n_c = \varepsilon_0\omega^2 m_e/e^2$, ε_0 is the dielectric constant. The temporal resolution $\Delta t = mc^{-1}(\Delta x^{-2} + \Delta y^{-2} + \Delta z^{-2})^{-1/2} = 4$ as, where $\Delta x = \Delta y = \Delta z = 0.025\,\mu m$ are the grid sizes in each direction and $m = 0.9$ is the time step factor. Open boundary conditions are employed for fields and particles.

According to Eqs. (1) and (2), the STOV electric fields were obtained in Fig. 1(d). The π-shift up and down fringes appear at the center of the STOV vortex beam ($z = 0\,\mu m$)

in the $x-z$ plane ($y = 0\,\mu m$), where the light phase fringes diminish and the light intensity is zero. In contrast, the up and down fringes connect far from the beam singularity ($z > 0\,\mu m$ and $z < 0\,\mu m$). Simultaneously, the fringe phase difference changes from π (for the center fringes) to 0. For the front and end parts of the STOV pulse, the phase structure is almost the same as that of the traditional Gaussian pulse [see Fig. 1(d)]. Such field and phase structures play important roles in the attosecond electron sheet generation in our case.

Figure 2 shows the attosecond electron sheet acceleration driven by the intense STOV pulse. The electrons are first dragged out of the nanowire target in the transverse direction and then pushed forward by a ponderomotive force [49], as shown in Fig. 2(a). Then, these electrons are dispersed by the front part of the STOV pulse, which has Gaussian-like field distributions [see Fig. 1(d)], corresponding to a dispersed ponderomotive force away from the z axis. In

contrast, an electron sheet was selected and concentrated in the intensity singularity of the STOV pulse by the corresponding hollow pondermotive force around the z axis at $t = 60T$ [see Fig. 2(c)]. This indicates that the spatiotemporal phase singularity in the STOV pulse is capable of providing another degree of spatiotemporal freedom for generating a single-electron sheet. Thus, this direct modulating method differs considerably from the traditional Gaussian laser-driven case.

The electrons in the center singularity can be compressed up to $\sim n_c$ in a sheet structure. Such an electron sheet is assumed to be simultaneously manipulated by the longitudinal and transverse fields of the STOV pulse near the singularity. On the one hand, the magnetic field prevents electrons from feeling the strong transverse electric fields (E_x and E_y), forming an electron concentration in the transverse direction [50]. On the other hand, the dipolar electric field (E_z) string manipulates the electrons on the z axis; the low-energy electrons are accelerated by the negative field at the back, and higher-energy electrons are decelerated by the positive field at the front. In our case, the STOV pulse with the proper initial phase can efficiently accelerate electrons in the same accelerated phase, thereby enabling the phase-locked acceleration for electrons. In addition, the electron sheet can be better collimated in the STOV pulse center because the maximum charge field generated by the electron sheet $E \sim 5.8 \times 10^{11}$ V/m is much smaller than the STOV pulse field ($\sim 2 \times 10^{14}$ V/m) in our case. Here, assuming the electron as a uniformly charged electric sheet with a radius of $R \sim 1\,\mu m$, the maximum electric field $E(r_E = R = 1\,\mu m)$ can be calculated by $q/(4\pi\varepsilon_0 R^2)$, where $q \sim 65$ pC is chosen. r_E is the radius and $\varepsilon_0 = 8.8542 \times 10^{-12}$ F/m is the dielectric constant. Finally, the concentrated electron sheet can be locked and further compressed at the front of the accelerating phase at $t = 110T$ [see Fig. 2(e)].

To obtain a clean attosecond electron sheet, a solid target can be placed behind the nanowire target at an oblique angle of 45° to reflect the defocused STOV pulse and prevent further interaction between the laser and the electrons at $t = 110T$ [51]. Then, such an attosecond electron sheet at the center can be further filtered out after a gating [52]. Finally, a RIAES (~ 670 as) can be continuously accelerated for at least 100 μm up to ~ 0.9 GeV with an $\sim 9\%$ energy spread, charge ~ 65 pC, and ~ 20 mrad divergence, which can be potentially applied to general fields that need spatiotemporal manipulation.

IV. NUMERICAL CALCULATION

To interpret the accelerating role of such a relativistic CP STOV pulse, the single-particle model was employed, which is a simplified numerical approach compared to the PIC simulation in Fig. 2. The particle acceleration can then be expressed as [22]

$$\dot{\boldsymbol{v}} = \frac{e}{m\gamma}\left[\boldsymbol{E} + \frac{1}{c}\boldsymbol{v}\times\boldsymbol{H} - \frac{1}{c^2}\boldsymbol{v}(\boldsymbol{v}\cdot\boldsymbol{E})\right]. \quad (4)$$

The electrons with the initial gamma factor ($\gamma_z \sim 7$) along the $+z$ direction were initially localized in the spatiotemporal phase singularity region and accelerated by the STOV pulse, where $\gamma_z = (1 - v_z^2/c^2)^{-1/2}$ and v_z is the electron velocity
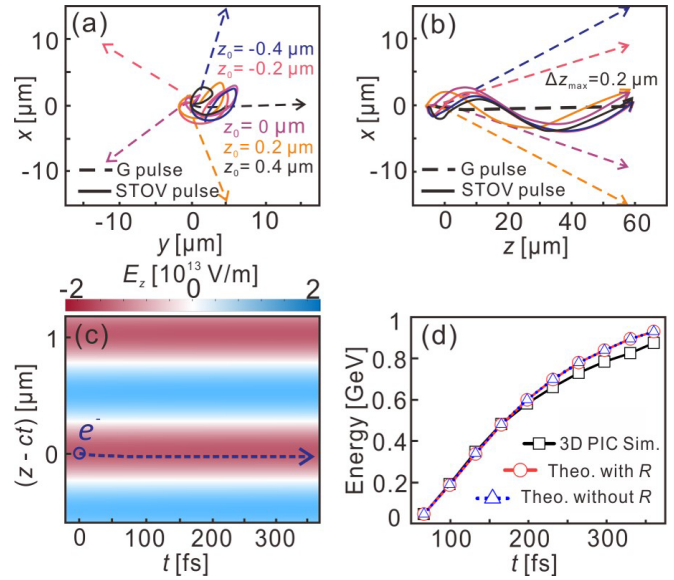

FIG. 3. 3D trajectories of electrons at different initial positions in the (a) y-x plane and (b) z-x plane for the STOV pulse and the Gaussian pulse. (c) The longitudinal position of a single electron relative to the longitudinal electric field. (d) Energy gain of the RIAES from 3D PIC (black square), and the prediction of the model without v_{ph} (blue triangle) and with v_{ph} (red circle).

along the z axis. Using Eq. (4), the trajectories of electrons at different initial positions ($-0.4\,\mu m < z_0 < 0.4\,\mu m$) were obtained in Figs. 3(a) and 3(b). All these electrons traveled along the z axis for 150 fs in the STOV pulse fields [see Fig. 3(b)] and collimated around the z axis, which is different from the Gaussian laser-driven case. Additionally, the initial separation between the electrons $\Delta z = 0.8\,\mu m$ can be compressed to $\Delta z = 0.2\,\mu m$ [see Fig. 3(b)]. Such compression results in the electron pulse duration to approximately 670 as, which is consistent with the case in the simulation in Fig. 2(c). This can be primarily attributed to electrons slipping into the same accelerated phase to achieve the phase-locked acceleration of the RIAES.

Furthermore, the electron trajectories were bent around the z axis [see Fig. 3(a)] because the electrons can be continuously rotated by the magnetic field within a Larmor radius $r_L = \gamma_x m_e v_x/eB_z$ in the zero-intensity region. Here, v_x is the electron velocity along the x axis, $\gamma_x = (1 - v_x^2/c^2)^{-1/2}$, and B_z is the longitudinal magnetic field. In our case, $r_L \sim 1\,\mu m$ was calculated for $B_z \sim 60$ kT and $\gamma_x = 35$, consistent with the electron radius in Fig. 2(c). These calculation results from the single-particle model (see Fig. 3) prove that the unique STOV fields in the singularity can produce RIAES.

Based on Eq. (4), the dephasing rate $R = (v_{ph} - v_z)/v_{ph}$ experienced by the accelerated electron in the longitudinal field E_z was used to explain the STOV laser-driven phase-locked acceleration progress in our case, where $v_{ph} = -(\partial\varphi/\partial t)/\nabla\varphi$ is the phase velocity of E_z, and $\nabla\varphi$ is the phase gradient along the particle trajectory. For simplicity, a single-electron motion initially at $z = 0\,\mu m$ was considered in the coordinate system of the phase velocity in the longitudinal field in the one-dimensional calculation. The electron gamma factor $\gamma_z = 1291$ can then be obtained at
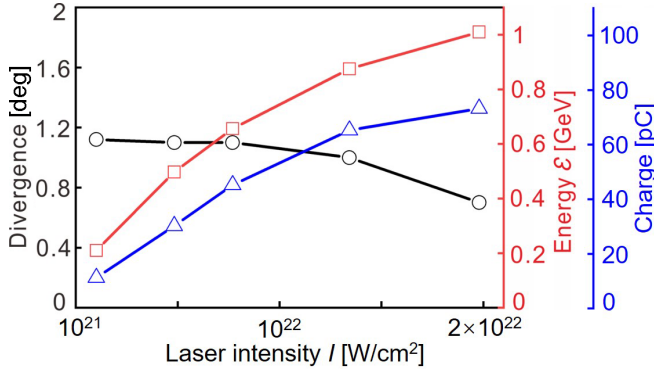
FIG. 4. Peak electron energy ε (red triangles), divergence (black circles), and charge (blue asterisks) of the RIAES as a function of laser intensity I. The laser duration and focal spot remain the same.

$t = 360$ fs from Fig. 3(c), and $v_{\mathrm{ph}} = c$ can be calculated using $v_{\mathrm{ph}} = -(\partial\varphi/\partial t)/\nabla\varphi$ for the STOV pulse in our case, so that a small value of $R = (c - v_z)/c = 4 \times 10^{-7}$ is obtained, indicating the electron is phase-lock accelerated.

Depending on the dephasing rate R and electric field E_z, we can also calculate the energy gain as $\Delta\varepsilon = -eE_z(1 - R)z$. It should be noted that R will change from 0.0004 at $t = 3.3T$ to 10^{-7} at $t = 360T$ when the electron velocity v_z continuously increases during the acceleration process. Therefore, we calculate $\Delta\varepsilon$ by integrating $d\varepsilon = -eE_z(1 - R)dt(z \approx ct)$ as

$$\Delta\varepsilon = -\int_0^{z/c} \frac{e(1 - R)E_z}{c} dt. \tag{5}$$

It was found that the calculated electron energy according to Eq. (5) agrees well with the PIC simulation result [see Fig. 3(d)]. In addition, the ideal situation without considering the dephasing rate ($R = 0$) can also be calculated as $\Delta\varepsilon = -\int_0^z (eE_z/c)dz$ and compared to our simulation results. Figure 3(d) shows that the electron energy is almost consistent with the PIC simulation, meaning that the electron can be stably phase accelerated by STOV pulse in our case.

V. DISCUSSION AND CONCLUSION

From the above discussion, it can be found that relativistic STOV pulses provide an efficient acceleration not only to generate an isolated attosecond electron sheet but also to reduce the beam divergence and energy spectrum in the DLA regime. With the development of 10-PW laser facilities, laser intensities can further increase up to 10^{22} W/cm^2. Figure 4 shows that the electron sheet energy and charge increase with the laser intensity I, because a higher longitudinal electric field can phase lock more electrons in the longitudinal electric field and accelerate them to the GeV order. At the same time, the beam divergence decreases with I, benefiting from the stronger magnetic field that confines electrons within a smaller Larmor radius. For $I = 2 \times 10^{22}$ W/cm^2 ($\sim$10 PW laser), the attosecond electron sheet can be accelerated to $\sim$1 GeV with an energy spectrum ($\sim$8%) while maintaining a low beam divergence of $\sim$14 mrad. Such high-energy electron sheets can be potentially applied for high-energy x/γ-ray sources [53], coherent synchrotron emission [54], and giant half-cycle attosecond pulse generation [38].

In conclusion, this study proposed a reflective manner for relativistic STOV pulse generation, which was applied to accelerate the RIAES in 3D PIC simulations. It was found that the spatiotemporal phase singularity in the STOV pulse is crucial to both concentrate and compress the electron sheet with high energy ($\sim$0.9 GeV), isolated attosecond ($\sim$670 as) duration, low-energy dispersion ($\sim$9%), low divergence angle ($\sim$20 mrad), and high charge ($\sim$65 pC). With the technological development in present PW lasers, such relativistic STOV pulse is hoped to be realized in laboratories soon, which may provide a new convenient method for accelerating a single attosecond electron sheet for attosecond electron diffraction, and microscopy, isolated attosecond pulse generation, ultrashort isolated x/γ-ray radiation, relativistic isolated electron mirrors, and other applications.

[1] L. Allen, M. W. Beijersbergen, R. J. C. Spreeuw, and J. P. Woerdman, Orbital angular momentum of light and the transformation of Laguerre-Gaussian laser modes, Phys. Rev. A **45**, 8185 (1992).

[2] K. Y. Bliokh and F. Nori, Spatiotemporal vortex beams and angular momentum, Phys. Rev. A **86**, 033824 (2012).

[3] S. L. Huang, P. Wang, X. Shen, J. Liu, and R. X. Li, Diffraction properties of light with transverse orbital angular momentum, Optica **9**, 469 (2022).

[4] S. W. Hancock, S. Zahedpour, A. Goffin, and H. M. Milchberg, Free-space propagation of spatiotemporal optical vortices, Optica **6**, 1547 (2019).

[5] A. Chong, C. Wan, J. Chen, and Q. Zhan, Generation of spatiotemporal optical vortices with controllable transverse orbital angular momentum, Nat. Photonics **14**, 350 (2020).

[6] C. H. Wan, Q. Cao, J. Chen, A. Chong, and Q. W. Zhan, Toroidal vortices of light, Nat. Photonics **16**, 519 (2022).

[7] M. E. J. Friese, J. Enger, H. Rubinsztein-Dunlop, and N. R. Heckenberg, Optical angular-momentum transfer to trapped absorbing particles, Phys. Rev. A **54**, 1593 (1996).

[8] A. B. Stilgoe, T. A. Nieminen, and H. Rubinsztein-Dunlop, Controlled transfer of transverse orbital angular momentum to optically trapped birefringent microparticles, Nat. Photonics **16**, 346 (2022).

[9] J. Wang, Advances in communications using optical vortices, Photonics Res. **4**, B14 (2016).

[10] I. Gianani, A. Suprano, T. Giordani, N. Spagnolo, F. Sciarrino, D. Gorpas, V. Ntziachristos, K. Pinker, N. Biton, J. Kupferman, and S. Arnon, Transmission of vector vortex beams in dispersive media, Adv. Photonics **2**, 1 (2020).

[11] A. Jesacher, S. Fürhapter, S. Bernet, and M. Ritsch-Marte, Shadow effects in spiral phase contrast microscopy, Phys. Rev. Lett. **94**, 233902 (2005).

[12] B. Jack, J. Leach, J. Romero, S. Franke-Arnold, M. Ritsch-Marte, S. M. Barnett, and M. J. Padgett, Holographic ghost imaging and the violation of a Bell inequality, Phys. Rev. Lett. **103**, 083602 (2009).

[13] F. Tamburini, B. Thidé, G. Molina-Terriza, and G. Anzolin, Twisting of light around rotating black holes, Nat. Phys. **7**, 195 (2011).

[14] S. W. Hancock, S. Zahedpour, and H. M. Milchberg, Second-harmonic generation of spatiotemporal optical vortices and conservation of orbital angular momentum, Optica **8**, 594 (2021).

[15] G. Gui, N. J. Brooks, H. C. Kapteyn, M. M. Murnane, and C. T. Liao, Second-harmonic generation and the conservation of spatiotemporal orbital angular momentum of light, Nat. Photonics **15**, 608 (2021).

[16] L. Rego, K. M. Dorney, N. J. Brooks, Q. L. Nguyen, C.-T. Liao, J. S. Román, D. E. Couch, A. Liu, E. Pisanty, M. Lewenstein, L. Plaja, H. C. Kapteyn, M. M. Murnane, and C. Hernández-García, Generation of extreme-ultraviolet beams with time-varying orbital angular momentum, Science **364**, eaaw9486 (2019).

[17] D. Strickland and G. Mourou, Compression of amplified chirped optical pulses, Opt. Commun. **56**, 219 (1985).

[18] C. N. Danson, C. Haefner, J. Bromage, T. Butcher, J.-C. F. Chanteloup, E. A. Chowdhury, A. Galvanauskas, L. A. Gizzi, J. Hein, D. I. Hillier, N. W. Hopps, Y. Kato, E. A. Khazanov, R. Kodama, G. Korn, R. Li, Y. Li, J. Limpert, J. Ma, C. H. Nam, D. Neely, D. Papadopoulos, R. R. Penman, L. Qian, J. J. Rocca, A. A. Shaykin, C. W. Siders, C. Spindloe, S. Szatmári, R. M. G. M. Trines, J. Zhu, P. Zhu, and J. D. Zuegel, Petawatt and exawatt class lasers worldwide, High Power Laser Sci. Eng. **7**, e54 (2019).

[19] W. P. Wang, C. Jiang, H. Dong, X. M. Lu, J. F. Li, R. J. Xu, Y. J. Sun, L. H. Yu, Z. Guo, X. Y. Liang, Y. X. Leng, R. X. Li, and Z. Z. Xu, Hollow plasma acceleration driven by a relativistic reflected hollow laser, Phys. Rev. Lett. **125**, 034801 (2020).

[20] G. F. Quinteiro, F. Schmidt-Kaler, and C. T. Schmiegelow, Twisted-light-ion interaction: The role of longitudinal fields, Phys. Rev. Lett. **119**, 253203 (2017).

[21] W. P. Wang, B. F. Shen, X. M. Zhang, L. G. Zhang, Y. Shi, and Z. Z. Xu, Hollow screw-like drill in plasma using an intense Laguerre-Gaussian laser, Sci. Rep. **5**, 1 (2015).

[22] W. P. Wang, C. Jiang, B. F. Shen, F. Yuan, Z. M. Gan, H. Zhang, S. H. Zhai, and Z. Z. Xu, New optical manipulation of relativistic vortex cutter, Phys. Rev. Lett. **122**, 024801 (2019).

[23] L. B. Ju, C. T. Zhou, T. W. Huang, K. Jiang, C. N. Wu, T. Y. Long, L. Li, H. Zhang, M. Y. Yu, and S. C. Ruan, Generation of collimated bright gamma rays with controllable angular momentum using intense Laguerre-Gaussian laser pulses, Phys. Rev. Appl. **12**, 014054 (2019).

[24] J. Wang, X. B. Li, L. F. Gan, Y. Xie, C. L. Zhong, C. T. Zhou, S. P. Zhu, X. T. He, and B. Qiao, Generation of intense vortex gamma rays via spin-to-orbital conversion of angular momentum in relativistic laser-plasma interactions, Phys. Rev. Appl. **14**, 014094 (2020).

[25] W. T. Wang, K. Feng, L. T. Ke, C. H. Yu, Y. Xu, R. Qi, Y. Chen, Z. Y. Qin, Z. J. Zhang, M. Fang, J. Q. Liu, K. N. Jiang, H. Wang, C. Wang, X. J. Yang, F. X. Wu, Y. X. Leng, J. S. Liu, R. X. Li, and Z. Z. Xu, Free-electron lasing at 27 nanometres based on a laser wakefield accelerator, Nature (London) **595**, 516 (2021).

[26] O. N. Rosmej, X. F. Shen, A. Pukhov, L. Antonelli, F. Barbato, M. Gyrdymov, M. M. Günther, S. Zähter, V. S. Popov, N. G. Borisenko, and N. E. Andreev, Bright betatron radiation from direct-laser-accelerated electrons at moderate relativistic laser intensity, Matter Radiat. Extremes **6**, 048401 (2021).

[27] A. Denoeud, L. Chopineau, A. Leblanc, and F. Quéré, Interaction of ultraintense laser vortices with plasma mirrors, Phys. Rev. Lett. **118**, 033902 (2017).

[28] J. Vieira, R. M. G. M. Trines, E. P. Alves, R. A. Fonseca, J. T. Mendonça, R. Bingham, P. Norreys, and L. O. Silva, High orbital angular momentum harmonic generation, Phys. Rev. Lett. **117**, 265001 (2016).

[29] X. M. Zhang, B. F. Shen, Y. Shi, X. M. Wang, L. G. Zhang, W. P. Wang, J. C. Xu, L. Yi, and Z. Z. Xu, Generation of intense high-order vortex harmonics, Phys. Rev. Lett. **114**, 173901 (2015).

[30] H. C. Wu, J. Meyer-ter-Vehn, J. Fernández, and B. M. Hegelich, Uniform laser-driven relativistic electron layer for coherent thomson scattering, Phys. Rev. Lett. **104**, 234801 (2010).

[31] V. V. Kulagin, V. A. Cherepenin, M. S. Hur, and H. Suk, Theoretical investigation of controlled generation of a dense attosecond relativistic electron bunch from the interaction of an ultrashort laser pulse with a nanofilm, Phys. Rev. Lett. **99**, 124801 (2007).

[32] W. J. Ma, J. H. Bin, H. Y. Wang, M. Yeung, C. Kreuzer, M. Streeter, P. S. Foster, S. Cousens, D. Kiefer, B. Dromey, X. Q. Yan, J. Meyer-ter-Vehn, M. Zepf, and J. Schreiber, Bright sub-cycle extreme ultraviolet bursts from a single dense relativistic electron sheet, Phys. Rev. Lett. **113**, 235002 (2014).

[33] N. Naumova, I. Sokolov, J. Nees, A. Maksimchuk, V. Yanovsky, and G. Mourou, Attosecond electron bunches, Phys. Rev. Lett. **93**, 195003 (2004).

[34] C. Jiang, W. P. Wang, H. Dong, Y. X. Leng, R. X. Li, and Z. Z. Xu, Collimated electron sheet driven by an intense Laguerre–Gaussian pulse, Phys. Plasmas **28**, 093102 (2021).

[35] F. F. Qi, Z. R. Ma, L. R. Zhao, Y. Cheng, W. X. Jiang, C. Lu, T. Jiang, D. Qian, Z. Wang, W. T. Zhang, P. F. Zhu, X. Zou, W. S. Wan, D. Xiang, and J. Zhang, Breaking 50 femtosecond resolution barrier in MeV ultrafast electron diffraction with a double bend achromat compressor, Phys. Rev. Lett. **124**, 134803 (2020).

[36] M. T. Hassan, J. S. Baskin, B. Liao, and A. H. Zewail, High-temporal-resolution electron microscopy for imaging ultrafast electron dynamics, Nat. Photonics **11**, 425 (2017).

[37] M. Gao, C. Lu, H. Jean-Ruel, L. C. Liu, A. Marx, K. Onda, S. Y. Koshihara, Y. Nakano, X. Shao, T. Hiramatsu, G. Saito, H. Yamochi, R. R. Cooney, G. Moriena, G. Sciaini, and R. J. D. Miller, Mapping molecular motions leading to charge delocalization with ultrabright electrons, Nature (London) **496**, 343 (2013).

[38] H. C. Wu and J. Meyer-ter-Vehn, Giant half-cycle attosecond pulses, Nat. Photonics **6**, 304 (2012).

[39] J. C. Xu, B. F. Shen, X. M. Zhang, Y. Shi, L. L. Ji, L. G. Zhang, T. J. Xu, W. P. Wang, X. Y. Zhao, and Z. Z. Xu, Terawatt-scale optical half-cycle attosecond pulses, Sci. Rep. **8**, 2669 (2018).

[40] K. Hu and H. C. Wu, Generation of gigawatt circularly polarized attosecond-pulse pairs, Phys. Rev. Lett. **119**, 254801 (2017).

[41] K. Hu and H. C. Wu, Enhanced coherent thomson scattering in the few-cycle regime, Opt. Lett. **41**, 4586 (2016).

[42] F. Krausz and M. Ivanov, Attosecond physics, Rev. Mod. Phys. **81**, 163 (2009).

[43] C. H. Shim, Y. W. Parc, S. Kumar, I. S. Ko, and D. E. Kim, Isolated terawatt attosecond hard x-ray pulse generated from single current spike, Sci. Rep. **8**, 7463 (2018).

[44] H. C. Wu and J. Meyer-ter-Vehn, The reflectivity of relativistic ultra-thin electron layers, Eur. Phys. J. D **55**, 443 (2009).

[45] D. Kiefer, M. Yeung, T. Dzelzainis, P. S. Foster, S. G. Rykovanov, C. L. Lewis, R. S. Marjoribanks, H. Ruhl, D. Habs, J. Schreiber, M. Zepf, and B. Dromey, Relativistic electron mirrors from nanoscale foils for coherent frequency upshift to the extreme ultraviolet, Nat. Commun. **4**, 1763 (2013).

[46] J. J. Zheng, C. H. Zhou, J. J. Feng, and B. Wang, Polarizing beam splitter of deep-etched triangular-groove fused-silica gratings, Opt. Lett. **33**, 1554 (2008).

[47] T. D. Arber, K. Bennett, C. S. Brady, A. Lawrence-Douglas, M. G. Ramsay, N. J. Sircombe, P. Gillies, R. G. Evans, H. Schmitz, A. R. Bell, and C. P. Ridgers, Contemporary particle-in-cell approach to laser-plasma modelling, Plasma Phys. Control. Fusion **57**, 113001 (2015).

[48] B. Richards and E. Wolf, Electromagnetic diffraction in optical systems, II. Structure of the image field in an aplanatic system, Proc. R. Soc. Lond. A **253**, 358 (1959).

[49] W. Wang, L. Xia, J. Xiong, Z. H. Fang, H. H. An, Z. Y. Xie, W. B. Pei, and S. Z. Fu, Field shaping and electron acceleration by center-depressed laser beams, Phys. Plasmas **26**, 093109 (2019).

[50] Y. Shi, D. Blackman, D. Stutman, and A. Arefiev, Generation of ultrarelativistic monoenergetic electron bunches via a synergistic interaction of longitudinal electric and magnetic fields of a twisted laser, Phys. Rev. Lett. **126**, 234801 (2021).

[51] C. Jiang, W. P. Wang, S. Weber, H. Dong, Y. X. Leng, R. X. Li, and Z. Z. Xu, Direct acceleration of an annular attosecond electron slice driven by near-infrared Ggaussian laser, High Power Laser Sci. Eng. **9**, 8 (2021).

[52] M. Kozak, All-optical scheme for generation of isolated attosecond electron pulses, Phys. Rev. Lett. **123**, 203202 (2019).

[53] K. Ta Phuoc, S. Corde, C. Thaury, V. Malka, A. Tafzi, J. P. Goddet, R. C. Shah, S. Sebban, and A. Rousse, All-optical compton gamma-ray source, Nat. Photonics **6**, 308 (2012).

[54] A. Pukhov, D. An der Brügge, and I. Kostyukov, Relativistic laser plasmas for electron acceleration and short wavelength radiation generation, Plasma Phys. Controlled Fusion **52**, 124039 (2010).